PAPER • **OPEN ACCESS**

Perchlorate-based poly(vinylidene fluoride-co-hexafluoropropylene) gel polymer electrolytes for high-voltage supercapacitors

To cite this article: Janhavi Sharma *et al* 2026 *Mater. Res. Express* **13** 125502

Materials Research Express

OPEN ACCESS

RECEIVED
6 May 2026

REVISED
31 May 2026

ACCEPTED FOR PUBLICATION
16 June 2026

PUBLISHED
26 June 2026

PAPER

Perchlorate-based poly(vinylidene fluoride-co-hexafluoropropylene) gel polymer electrolytes for high-voltage supercapacitors

Janhavi Sharma[1], **Marcin Krajewski**[1,*], **Chandra Shekhar**[2], **Kamil Bochenek**[1], **Angelika Zaszczyńska**[1], **Emerson Coy**[3], **Marcin Jarek**[3], **Zhi-Ting Huang**[4] **and Amrita Jain**[1,*]

[1] Institute of Fundamental Technological Research, Polish Academy of Sciences, Pawińskiego 5B, Warsaw 02-106, Poland
[2] Department of Chemical Engineering, Thapar Institute of Engineering and Technology, Patiala, Punjab 147004, India
[3] NanoBioMedical Centre, Adam Mickiewicz University, Wszechnicy Piastowskiej 3, 61-614 Poznan, Poland
[4] Department of Chemical and Materials Engineering, Tunghai University, No. 181, Sec. 3, Taichung Port Rd., Taichung 40704, Taiwan, ROC
[*] Authors to whom any correspondence should be addressed.

E-mail: mkraj@ippt.pan.pl and ajain@ippt.pan.pl

Keywords: activated carbon, gel polymer electrolyte, ionic conductivity, supercapacitor, temperature dependence

Supplementary material for this article is available online

Abstract

This study explores the development of porous poly(vinylidene fluoride-co-hexafluoropropylene) based gel polymer electrolytes (GPEs) via a general polyethylene glycol extraction method, followed by the incorporation of perchlorate salts ($LiClO_4$, $Mg(ClO_4)_2$, $NaClO_4$). The influence of cation valency and ionic radius on ionic transport was systematically investigated for high-voltage supercapacitors (SCs). Among the prepared electrolytes, the $LiClO_4$ based GPE exhibits the highest ionic conductivity of 7.4×10^{-3} S cm^{-1} at room temperature along with a stable electrochemical window of 2.6 V and superior performance in symmetric SCs. Symmetric SCs assembled with activated carbon achieved a specific capacitance of 76.7 F g^{-1} and retained excellent cycling stability of 96.9% after 10 000 consecutive charge-discharge cycles measured at a current density of 1 A g^{-1}. This work highlights the enhanced performance of ion transport attributed to a well-interconnected porous structure at the electrode−electrolyte interface and provides insights into the role of chemistry in high-performance SCs.

1. Introduction

In the modern era, it is almost inconceivable to anticipate daily life without ready access to on-demand electricity. The depletion of fossil fuel resources and concerns about global warming are driving the shift towards electricity storage. In general, the approach is to accumulate electricity when it is accessible and distribute it when needed [1]. The international energy agency has reported that global energy demand is expected to grow by 2% annually, gradually reaching 78% by 2050 [2]. The rising demand for energy storage solutions has led to the development of energy storage devices that combine high power density, quick charge-discharge capability, and long-lasting stability [3].

Among the various energy storage devices, supercapacitors (SCs), especially electrical double-layer capacitors (EDLCs), appear promising owing to their high power density, excellent cycling stability, and fast charge-discharge kinetics [4]. Despite these advantages, the major challenges towards the widespread application of SCs in next-generation applications are limited by the development of electrolytes, as conventional liquid electrolytes struggle with the issues of leakage, flammability, and limited electrochemical stability [5]. To address these limitations, gel polymer electrolytes (GPEs) have emerged as an alternative, combining the mechanical stability of solid electrolytes with the high ionic conductivity of liquid systems [6]. Furthermore, GPE is well—suited for flexible and miniaturized mobile devices [7].

Recent studies indicate that GPEs with poly(vinylidene fluoride-co-hexafluoropropylene) (PVDF-HFP) as a host material exhibit excellent electrochemical stability, fire resistance, and compatibility for application with various electrode materials, thus marking it as a frontrunner in applications of

advanced SCs, and are widely investigated in SC applications [8, 9]. The semicrystalline nature of PVDF-HFP, consisting of crystalline PVDF regions and amorphous HFP domains, enables a balance between mechanical strength and ion transport [10]. PVDF has remarkable properties such as high thermal stability, a wide voltage window, and electrochemical stability; however, owing to its rigid crystalline structure, it restricts solvent uptake and limits the intrinsic ionic conductivity of pure PVDF [11]. In contrast, the co-polymer PVDF-HFP reduces the crystallinity, creating amorphous phases and a microporous structure within the polymer matrix, ultimately boosting electrolyte uptake, ionic conductivity, flexibility, and interfacial compatibility, which are critical for GPE applications [12]. Additionally, it has been observed with several studies that PVDF acts as a non-coordinating polymer with lithium salts, whereas in PVDF-HFP, the salt clusters form a percolating network, creating channels for hopping from one stable position to another. In addition, PVDF-HFP possesses better film-forming properties and mechanical flexibility than PVDF while maintaining excellent electrochemical stability and chemical resistance. These advantages make PVDF-HFP particularly suitable for solid-state SCs [13].

Despite the aforementioned advantages, the ionic conductance and interfacial compatibility must be enhanced in GPEs to meet the criteria for high-performance SCs [14]. One effective strategy involves introducing controlled porosity into the GPE to facilitate electrolyte uptake and ion transport. Conventional pore-forming strategies, such as salt-leaching, hard-template removal, thermally/solvent-induced phase separation, and template etching, often involve complex processing steps or limited scalability. The selective removal of polyethylene glycol (PEG) from PVDF-HFP matrices is a relatively new approach to promote porosity, facilitating electrolyte uptake and ion scattering in a relatively more efficient manner, offering a simple and cost-effective route through selective solvent extraction by avoiding multi-step template procedures [15, 16]. Among various pore-forming agents, such as PVP, water, LiCl, and $ZnCl_2$, PEG serves as a sacrificial pore-forming agent (porogen) [17]. During membrane fabrication, PEG was homogeneously mixed with PVDF-HFP. Subsequent methanol extraction selectively removed PEG from the polymer matrix, leaving behind interconnected porous channels [18]. These porous structures enhance electrolyte uptake, increase the number of amorphous regions, improve ion diffusion pathways, and facilitate ionic transport throughout the membrane [19]. The PEG content also influences the pore density and morphology, thereby directly affecting the ionic conductivity and mechanical behavior. This approach is also cost-effective, simple, and scalable, avoiding the need for multi-step template procedures [20].

Despite significant progress in PVDF-HFP-based GPEs for SC applications, most reported systems rely on conventional one-step fabrication approaches, in which the polymer matrix, salt, and plasticizer are introduced simultaneously. Such methods often limit the independent control over the electrolyte morphology and ion transport behavior, making it difficult to establish clear structure–property relationships. In addition, prior studies have predominantly focused on single-cation systems, with limited systematic comparisons of mono- and multivalent ions within the same polymer framework. Consequently, the fundamental influence of cation valency and ionic radius on ionic conductivity and electrochemical performance remains insufficiently understood. Furthermore, although porous architectures have been shown to enhance electrolyte uptake and ion mobility, the role of well-defined interconnected pore structures in modulating multivalent ion transport has not been comprehensively explored.

To address these gaps, in this work, we demonstrated an interesting approach for the synthesis of high-performance GPEs by engineering porous PVDF-HFP-based membranes through a synergistic combination of PEG and cation salt doping with lithium perchlorate ($LiClO_4$), magnesium perchlorate ($Mg(ClO_4)_2$), and sodium perchlorate ($NaClO_4$). Although TFSI salts are well known for their excellent electrochemical stability and ionic dissociation, perchlorate salts were selected in this work because of their comparatively lower cost, high ionic conductivity, high solubility in propylene carbonate (PC), and simpler ion dissociation behavior [21]. Furthermore, ClO_4^- anions possess relatively weak ion-pairing tendencies, which facilitate ion transport in polymer matrices. This study systematically investigated the influence of cation valency and ionic radius within a consistent perchlorate anion framework [22]. The methanol-assisted removal of PEG enabled the formation of hierarchically porous structures, promoting enhanced electrolyte uptake and ion transport in the formed structure. This approach allows for a direct and systematic investigation of cation-dependent transport phenomena within a consistent porous PVDF-HFP matrix, providing new insights into the interplay between morphology, ion properties, and electrochemical performance in high-voltage SCs.

Future aspects related to in-service conditions have also been verified by mechanical testing, which results in the stress–strain behavior of the obtained materials [23]. Finally, the results shown in this work demonstrate that a combination of porosity control and salt infiltration greatly improves the charge storage capacity and maintains the structural durability of perchlorate-based PVDF-HFP electrolytes. These advances make them promising GPEs for high-power energy storage SCs.

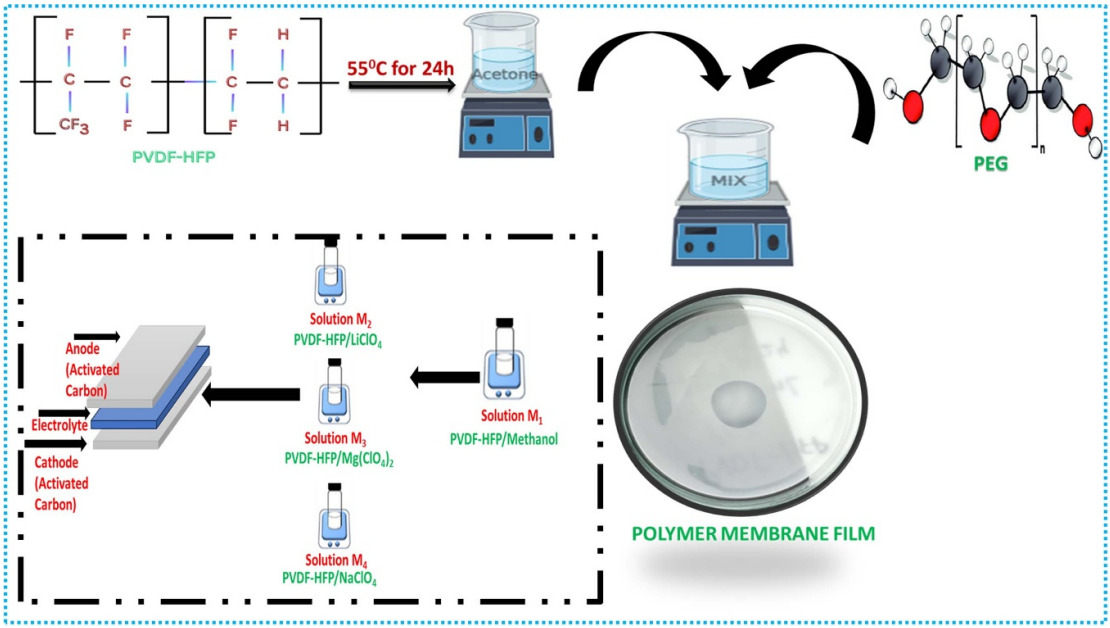

Figure 1. Schematic for the preparation of perchlorate-based PVDF-HFP gel polymer electrolyte films.

2. Experimental details

2.1. Materials used

PVDF-HFP ($M_w \sim 455\ 000$ g mol^{-1}) used as a host polymer for membrane preparation was purchased from Sigma Aldrich. PEG ($M_w \sim 400$ g mol^{-1}) was supplied by POCH chemicals. Acetone was used as the solvent in this study and was sourced from Linegal Chemicals. Lithium perchlorate ($LiClO_4$), magnesium perchlorate ($Mg(ClO_4)_2$), and sodium perchlorate ($NaClO_4$) salts were obtained from Thermo Scientific. Additionally, PC, used as the solvent for the preparation of perchlorate salt solutions, was supplied by Roth Chemicals. Styrene-butadiene rubber (SBR; 50−60 wt% SBR dispersed in H_2O) and activated carbon (AC; ACS20) were obtained from Grand Chemical Co., while carboxymethyl cellulose (CMC; $M_w = 250\ 000$ g mol^{-1}) was delivered by UNI-ONWARD Co. A titanium foil with a thickness of 20 μm for the current collector was supplied by UBIQ Technology Co. Ltd.

Please note that all chemicals were used as-received without undergoing any further purification.

2.2. Preparation of GPE films

GPEs were prepared according to the scheme shown in figure 1. The fabrication involved two steps: (i) preparation of porous PVDF-HFP membranes and (ii) incorporation of perchlorate salt electrolytes in the porous membrane.

The first step involves the formation of a polymer membrane using the pore-forming template method, in which the host PVDF-HFP polymer is mixed with PEG and the membrane is synthesized using a standard casting technique. In this process, 1.0 g of PVDF-HFP was dissolved in 20 ml of acetone for 24 h under magnetic stirring at 55 °C. Subsequently, different amounts of PEG ranging from 1 ml to 5 ml were added to the previously prepared PVDF-HFP solution. The resulting mixtures were again subjected to the magnetic stirring for 24 h at 55 °C. Prepared homogenous solutions were poured into glass petri dishes and dried in a fume chamber under ambient conditions to evaporate acetone for 24 h. After that, the dried PVDF-HFP-PEG films were soaked in methanol for 24 h to remove the PEG from the membrane which allows the formation of the pores structure. This process allowed for the development of pores via solvent extraction-induced phase separation. The second step involves the incorporation of perchlorate salt electrolytes in the synthesized porous membrane. Which involves the preparation of 1 M salt solutions containing $LiClO_4$, $Mg(ClO_4)_2$, and $NaClO_4$ separately dissolved in PC to form solvated cations $[M(PC)_n]^+$ with free ClO_4^-. They were stirred for 5 h at room temperature to ensure their homogeneity. Further, the previously obtained porous membranes were immersed in the respective salt solutions for 24 h to produce GPEs filled with different perchlorate salts. These electrolytes were prepared through the physical method instead of a chemical mechanism, which provides

a simple and low-cost process, enabling high perchlorate salt uptake. A visual representation of a free-standing polymer gel electrolyte is provided in the supplementary materials (see figure S1), highlighting its flexibility by showing its ability to twist, fold, and bend without fracture. The obtained GPEs were tested for SC application with activated carbon as electrode material.

2.3. Instrumental details

The morphologies of the prepared films were investigated with a scanning electron microscopy (SEM)/FIB-Zeiss Crossbeam 350 field emission-SEM equipped with an Ametek EDAX, Octane Elite energy dispersive spectrometer. Prior to imaging, a thin layer of gold was deposited on the sample to improve the electronic conductivity of the films. Fourier transform infrared (FTIR) with ATR technique was used to analyze the surface group of the synthesized films in the range of 400–4,000 cm^{-1}, with a resolution of 2 cm^{-1} and 32 scans. To analyze molecular vibrations in GPEs, the Raman studies were performed using a confocal Raman spectrometer (Renishaw inVia) equipped with a charge-coupled device camera and a continuous-wave diode-pumped Nd: YAG laser working at $\lambda = 785$ nm. The Raman spectra were collected between 400 and 3,400 cm^{-1} with the laser power of 5 mW. The crystallization temperature (T_C) and crystallinity (X_C) of PVDF-HFP membranes were determined with a differential scanning calorimetry (DSC) method using a DSC 8000 (PerkinElmer). Experiments were performed on samples closed in aluminum pans. The DSC runs were recorded during heating and cooling in the temperature range from 0 to 200 °C with a heating/cooling rate of 10 °C min^{-1}. Then, the analysis of obtained data was performed using THERMAL ANALYSIS Pyris Software (Version 13.3.2.0030, PerkinElmer). The mechanical properties of the prepared films were examined using stress–strain curves obtained by the Kammrath-Weiss module with a highly sensitive 50 N load cell and a maximum displacement rate equal to 20 μm s^{-1}.

The electrochemical studies were performed using the BioLogic VMP3 or SP-50e instruments. The electrochemical impedance spectroscopy technique (EIS) was used to evaluate the ionic conductivity (σ) of the GPEs in the frequency range of 1 Hz–200 kHz with a signal range of 10 mV. In order to record the data, the electrolytes were sandwiched between two stainless steel (SS) sheets (SS|electrolyte|SS). The σ of the GPEs is then evaluated using equation (1):

$$\sigma = \frac{1}{RA} \tag{1}$$

where l is the thickness of the polymer film, R is the bulk resistance of the cell, and A is the cross-sectional area that comes in contact with polymer electrolytes (in the present case, the area was 1 cm^2).

The uptake of perchlorate salts by porous membrane was verified by soaking the porous PVDF-HFP membranes in salts for 24 h and calculated with equation (2):

$$\text{perchlorate salt uptake}\,\% = \frac{m_{\text{PVDF-HFP+salt}} - m_{\text{PVDF-HFP}}}{m_{\text{PVDF}} - H_{\text{FP}}} \times 100\% \tag{2}$$

where $m_{\text{PVDF-HFP+salt}}$ corresponds to the weight of PVDF-HFP membrane after soaking in perchlorate salt, and $m_{\text{PVDF-HFP}}$ refers to the weight of porous PVDF-HFP obtained after PEG removal.

For temperature dependence measurements, an *in situ* experimental setup was used to test the ionic conductivity with temperature variation. The experiments were performed in an atmospheric chamber (CTS climate temperature system, type C-20/350, CTS Germany, series number 107 073), which was combined with the SP-50e BioLogic Instrument. The ionic conductivity was recorded while the temperature varied from 25 to 80 °C at a rate of 5 °C. Three readings were recorded at each scaled temperature and the average was used for analysis. The ionic conductivity of the GPE films was calculated using equation (1) at each temperature point.

2.4. Electrode preparation and SC cell assembly

To evaluate the practical availability of obtained GPEs, the EDLC cells were prepared by using commercially available AC as electrodes. To prepare them, a mixture containing 80 wt% AC, 10 wt% acetylene black, 10 wt% CMC and SBR in a 1:1 mass ratio was dissolved in acetone and stirred for 2 h at room temperature to obtain the homogenous solution. The resulting solution was cast onto titanium foil to obtain an electrode with a thickness of approximately 200 μm. The carbon-coated titanium foils were then dried in a vacuum oven at 120 °C for 12 h. Further, they were cut into discs with an average loading mass of 1.3 mg and an area of about 1 cm^2. A two-electrode configuration was employed in this work, where the as-prepared GPEs were sandwiched between two symmetrical AC electrodes and coin cells (CR2032) to prepare the electrochemical devices. The cell configurations were as follows:

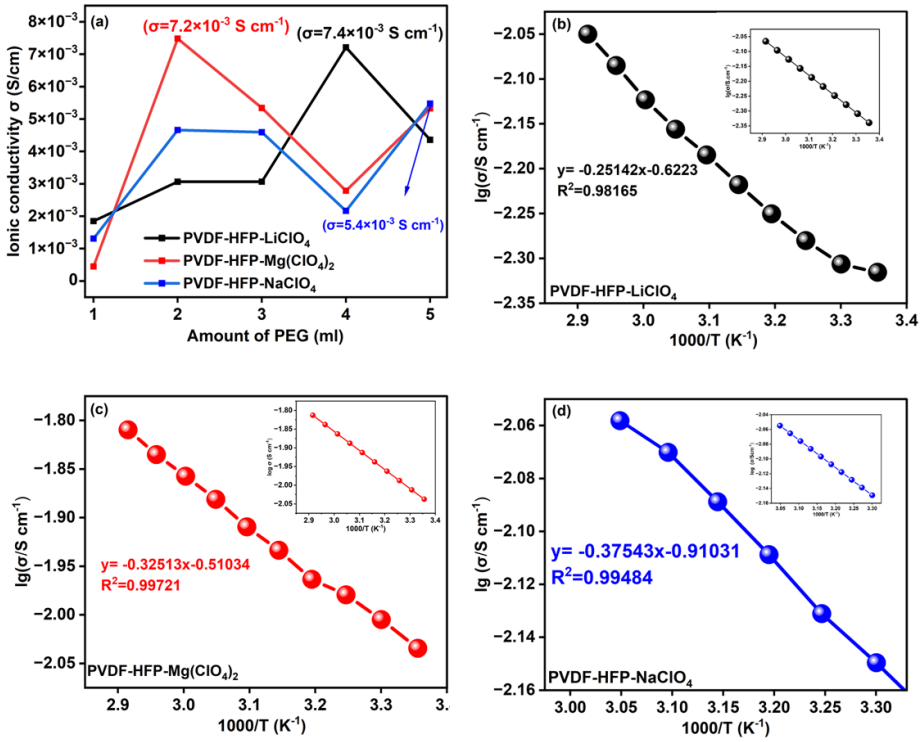

Figure 2. (a) Variation of ionic conductivity σ (S cm^{-1}) of PVDF-HFP-$LiClO_4$, PVDF-HFP-$Mg(ClO_4)_2$, and PVDF-HFP-$NaClO_4$ GPEs. Variation of ionic conductivity as a function of temperature recorded for (b) PVDF-HFP-$LiClO_4$, (c) PVDF-HFP-$Mg(ClO_4)_2$, and (d) PVDF-HFP-$NaClO_4$ GPEs (insets of figures 2(b)–(d) display the linear fitting of experimental data according to the Arrhenius relation).

Cell A: AC|PVDF-HFP-$LiClO_4$|AC

Cell B: AC|PVDF-HFP-$Mg(ClO_4)_2$|AC

Cell C: AC|PVDF-HFP-$NaClO_4$|AC

The electrochemical performance of the fabricated cells was evaluated using cyclic voltammetry (CV), EIS, galvanostatic charge-discharge (GCD) testing with repeated long-term cycling testing and Coloumbic efficiency of the cells. The details of the measurements, along with the mathematical expressions used to calculate capacitance values from each of the techniques, power densities, and energy densities were provided in the supplementary materials (equations (S1)−(S5)).

3. Results and discussion

3.1. Determination of ionic conductivity and electrochemical stability window (ESW)

The GPE films were prepared according to the scheme shown in the experimental section. The σ of salt-loaded GPEs were prepared using different PVDF-HEP (g): PEG (ml) composition by employing 1.0 g of PVDF-HFP and 1–5 mL of PEG corresponding to formulations denoted as 1:1, 1:2, 1:3, 1:4, 1:5. The ionic conductivity of the salt-loaded GPE films was measured at room temperature after electrolyte uptake [24]. The variation of σ with respect to different volume ratios of PEG is shown in figure 2(a). Which shows the highest value of σ for the $LiClO_4$, $Mg(ClO_4)_2$, and $NaClO_4$ salts was found at the ratios at 1:4, 1:2, and 1:5 (PVDF-HFP: PEG), as 7.4×10^{-3}, 7.2×10^{-3}, and 5.4×10^{-3} S cm^{-1}, respectively. The optimal PVDF-HFP: PEG ratio depends on the interplay between pore morphology, electrolyte uptake, ion size, charge density, and ion-polymer interactions for each specific salt system. Different cations exhibit distinct solvation behavior and interactions with the polymer matrix, which influence the balance between ionic transport and mechanical integrity. For example, Mg^{2+} possesses higher charge density and stronger ion-polymer coordination, enabling effective ion transport even at comparatively lower porosity (1:2 ratio). In contrast, Na^{+} requires a higher porosity (1:5 ratio) to compensate for its lower charge density and larger ionic radius. Although Mg^{2+} has lower mobility due to stronger coordination and divalent charge, its higher charge density may promote stronger ion–dipole

Table 1. Cationic and anionic transference numbers of optimized perchlorate-based PVDF-HFP GPEs.

GPE	t_+	t_-
PVDF-HFP-$LiClO_4$ (1:4)	0.7	0.3
PVDF-HFP-$Mg(ClO_4)_2$ (1:2)	0.5	0.5
PVDF-HFP-$NaClO_4$ (1:5)	0.4	0.6

interactions and salt dissociation, resulting in ionic conductivity comparable to that of the Li-based GPE [25]. The electrolyte with the lowest ionic conductivity was recorded for PVDF-HFP filled with $NaClO_4$ due to a low charge density of sodium ions as well as the largest Na ion radius among the investigated salts [26]. Since the optimized compositions of PVDF-HFP containing different perchlorate salts have been determined from the application point of view, further detailed characterizations were performed only for them [27].

To evaluate the ion transport behavior of GPEs under optimized conditions, the σ of the optimized films was recorded in the temperature range from 25 to 80 °C, and the recorded patterns are presented in figures 2(b)–(d) along with insets representing the linear fitting region of Arrhenius plots. As can be seen, the Li—and Mg-based GPEs exhibited a continuous increase in conductivity up to 70 °C, whereas the Na-based GPE showed stable conductivity behavior only up to approximately 60 °C. Which is an acceptable temperature range for the device fabrication and operation. The insets of figures 2(b)–(d) represent the Arrhenius behavior for the optimized electrolytes [28]. These plots demonstrate the thermal behavior of electrolytes with increasing σ in a linear relation to temperature. These trends represent the free volume expansion and the hopping mechanism between the coordinating sites and the segmental motion of polymer chains [29]. An increment in σ with respect to temperature represents the amorphization of the polymer structure and enhances ion hopping within the polymer framework. This phenomenon is further supported by the data presented in table S1, which summarizes the activation energy (E_a) values calculated using equation (3) for each optimized film, along with the corresponding ionic conductivity (σ) at room and elevated temperatures for PVDF-HFP-$LiClO_4$, PVDF-HFP-$Mg(ClO_4)_2$, and PVDF-HFP-$NaClO_4$ GPEs,

$$\sigma = \sigma_0 \exp\left(-\frac{E_a}{K_B T}\right) \tag{3}$$

where σ_0 is the ionic conductivity at absolute temperature, T corresponds to the measurement temperature, and k_B refers to the Boltzmann constant. The lowest E_a is found for PVDF-HFP-$LiClO_4$ GPE, while the highest one is for PVDF-HFP-$NaClO_4$ GPE.

Further, to evaluate the ion transport behavior of the optimized GPEs, cationic transference numbers (t_+) and anionic transference numbers (t_-) were measured using the EIS technique in the range from 100 Hz to 1 mHz and equations (4) and (5):

$$t_+ = \frac{I_S(\Delta V - I_0 R_0)}{I_0(\Delta V - I_S R_S)} \tag{4}$$

$$t_- = 1 - t_+ \tag{5}$$

where R_0 and R_S are the impedance before and after polarization, I_0 and I_S are the initial and final values of the variation of steady-state current, and ΔV is the constant voltage value of 10 mV. table 1 summarizes the calculated t_+ and t_- values for all optimized perchlorate-based PVDF-HFP GPEs. The moderate cation transference numbers indicate that ion transport is supported by both solvated-ion diffusion and hopping mechanisms within the amorphous regions of PVDF-HFP. The variation in transference numbers among the different salts used in this work highlights the strong impact of the cation type on the ion transport and conductivity of the investigated electrolytes. The obtained results demonstrate that the Li-based GPE is more suitable for applications requiring high cationic transport, whereas Na and Mg-based GPEs are relevant for anionic or balanced transport behavior. However, the higher value of the Li-based GPE suggests more favorable cationic contribution to charge transport, which may help reduce concentration polarization and improve rate performance [30]. Among the investigated electrolytes, PVDF-HFP-$LiClO_4$ shows the most favorable combination of high ionic conductivity and cation transference number.

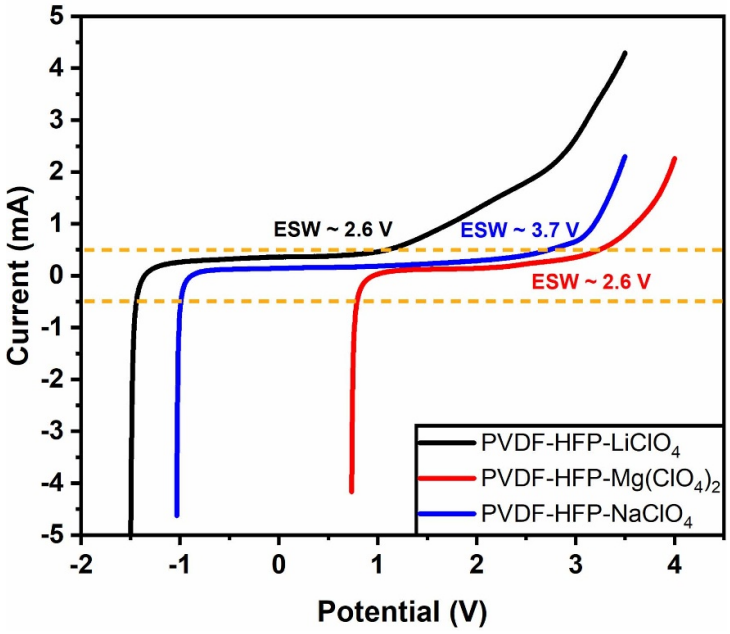

Figure 3. Electrochemical stability window plots of PVDF-HFP-$LiClO_4$, PVDF-HFP-$Mg(ClO_4)_2$, and PVDF-HFP-$NaClO_4$ GPEs.

Another important parameter associated with electrolytes is their ESW. This parameter defines the voltage range of an electrolyte, in which undesirable redox reactions do not occur. To evaluate the stability potential range of GPEs, linear sweep voltammetry (LSV) was conducted using a cell configuration of SS | electrolyte | SS. The optimized films were tested in the range from −4.0 V to +4.0 V at room temperature. The recorded LSV graphs shown in figure 3 indicate that all investigated GPEs exhibit ESWs of at least ∼2.6 V. In this context, stable electrochemical operation above a voltage window of ∼2–2.2 V is considered generally high because of their polymer matrix, ion transport limitations, which often restrict the practical operational window observed at 2.6 V rather than liquid electrolytes. The highest value of ESW is found for the PVDF-HFP containing $NaClO_4$ (∼3.7 V), while the ESWs for membranes filled with $LiClO_4$ and $Mg(ClO_4)_2$ are similar and greatly lower (∼2.6 V). The wider ESW of the $NaClO_4$-based electrolyte is likely due to the relatively lower reactivity and weaker interactions of Na^+ ions with the solvent and polymer matrix under high-voltage conditions [31, 32]. However, Na^+ ions have a larger ionic radius and lower charge density than Li^+ ions, leading to reduced ion mobility and slower charge transport within the polymer network. In addition, weaker ion dissociation and increased ionic friction contribute to the lower ionic conductivity observed for the $NaClO_4$-based system. Thus, although $NaClO_4$ improves voltage stability, its transport kinetics remain inferior to those of the $LiClO_4$-based GPE [33, 34].

3.2. Morphological, structural, and temperature dependence studies

To confirm the formation of porous PVDF-HFP structures and filling them with perchlorate-based salts, the SEM measurements were performed for different PVDF-HFP-to-PEG ratios (1:1, 1:2, 1:3, 1:4, 1:5). figure 4, shows the SEM images of optimized films, whereas other images are presented in the supplementary materials (cf. figures S2–S6). In turn, figures S7–S9 display the EDS elemental mapping for the optimized GPEs, which, apart from the Li-containing GPE, confirm the successful incorporation of Mg^{2+} and Na^+ ions. In the case of the PVDF-HFP-$LiClO_4$ sample, no signal related to lithium was captured because this element is too light to be detected with the EDS technique. The pristine PVDF-HFP-PEG membranes shown in figures 4(a), (d), (g) exhibit smooth, almost non-porous morphologies, which are characteristic for homogeneous polymer blends. Upon PEG extraction (figures 4(b), (e), (h)), a well-defined interconnected porous network emerges due to the dissolution of PEG in methanol, leaving behind high-surface-area matrices. As can be seen, the formation of a porous structure in PVDF-HFP matrices has been confirmed after the removal of PEG, allowing the introduction of salt into them. Figures 4(c), (f), and (i) present the PVDF-HFP filled with $LiClO_4$, $Mg(ClO_4)_2$, and $NaClO_4$ salts, respectively. SEM analysis confirmed the formation of interconnected porous structures after PEG extraction, which enhanced electrolyte uptake and facilitated ion transport pathways. The salt-filled porous networks observed in SEM images directly support the improved ionic conductivity results. To

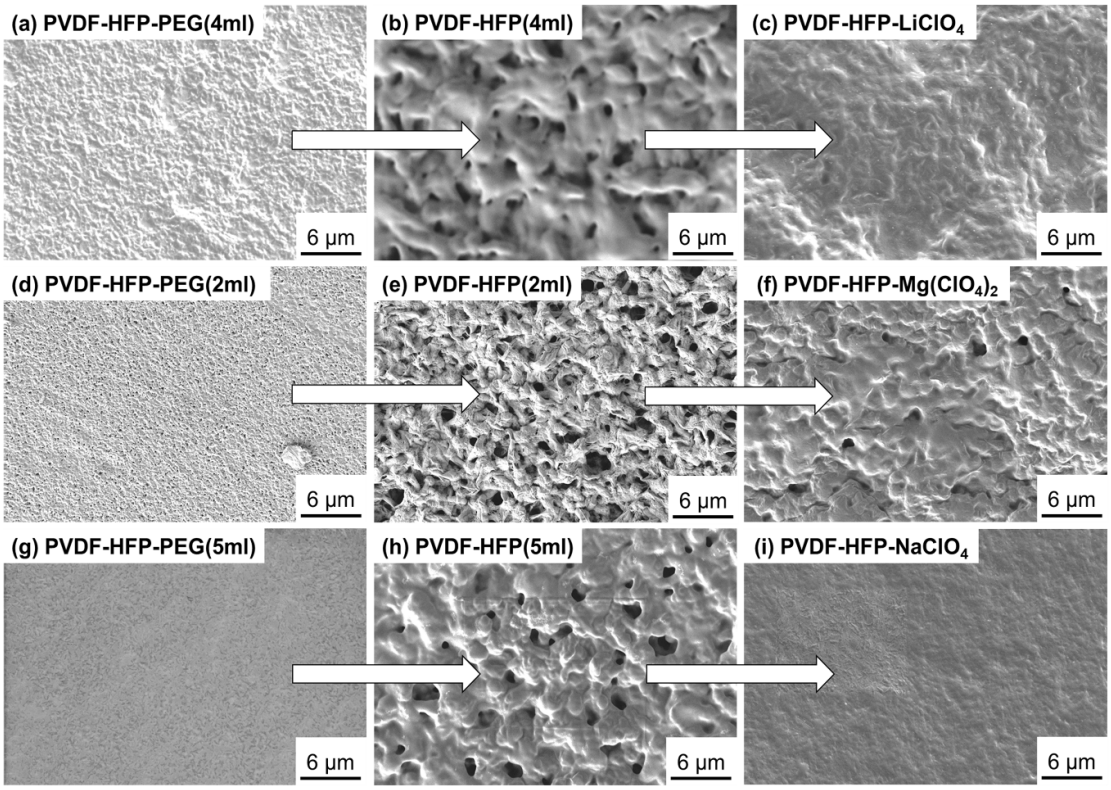

Figure 4. SEM images of (a) PVDF-HFP-PEG(4 ml), (b) porous PVDF-HFP(4 ml), (c) PVDF-HFP-$LiClO_4$, (d) PVDF-HFP-PEG(2 ml), (e) porous PVDF-HFP(2 ml), (f) PVDF-HFP-$Mg(ClO_4)_2$, (g) PVDF-HFP-PEG(5 ml), (h) porous PVDF-HFP(5 ml), and (i) PVDF-HFP-$NaClO_4$.

Table 2. Summary of mass variations of the optimized PVDF-HFP membranes during the fabrication of various GPEs.

GPE	$m_{\text{PVDF-HFP+PEG}}$ (mg)	$m_{\text{PVDF-HFP}}$ (mg)	$m_{\text{PVDF-HFP+perchlorate}}$ (mg)	Perchlorate salt uptake (%)
PVDF-HFP-$LiClO_4$ (1:4)	49.3	43.5	85.7	97
PVDF-HFP-$Mg(ClO_4)_2$ (1:2)	88.7	82.4	132.4	60.7
PVDF-HFP-$NaClO_4$ (1:5)	40.7	33.4	67.1	100

further investigate the porous characteristics of the prepared PVDF-HFP membranes after PEG extraction, Brunauer–Emmett–Teller surface area analysis was performed to evaluate the pore size distribution trends. The pore structure of PVDF-HFP films after PEG extraction strongly depended on the polymer-to-PEG ratio. At lower PEG content (1:2), the mechanically stable PVDF-HFP matrix preserved larger pores after extraction, resulting in an average pore size of 4.15 nm. Increasing PEG concentration to 1:4 reduced the pore size to 2.1 nm due to partial shrinkage and densification of the porous structure. At the highest PEG loading (1:5), excessive PEG removal weakened the polymer framework, leading to pore collapse and highly restricted accessible porosity, reflected by the very low apparent pore size of 0.27 nm.

The information related to the perchlorate salt uptake for the optimized GPEs measured using equation (2) is provided in table 2, while the salt-uptake behavior of GPE incorporating $LiClO_4$, $Mg(ClO_4)_2$, and $NaClO_4$ at ratios ranging from 1:1 to 1:5 is included in table S2 in the supplementary materials. The data collected in both tables basically confirms that the method of porosity control and salt introduction into the porous PVDF-HFP membrane is valid for various perchlorate salts. Moreover, it is also observed that the increasing content of PEG added during the synthesis causes the formation of networks with well-developed pores inside the host PVDF-HFP films, which allows for higher perchlorate salt uptake.

Both FTIR and Raman spectroscopy are used to confirm the complete extraction of PEG from PVDF-HFP, and filling the resulting pores with various perchlorate-based salts dissolved in PC. Figures 5(a) and (b) show the comparative FTIR and Raman spectra of pure PVDF-HFP, PVDF-HFP-PEG(4 ml), porous PVDF-HFP(4 ml), PVDF-HFP-$LiClO_4$, PVDF-HFP-$Mg(ClO_4)_2$, and PVDF-HFP-$NaClO_4$, while more detailed spectra are depicted in figure S10. Further, tables S3 and S4 provide the

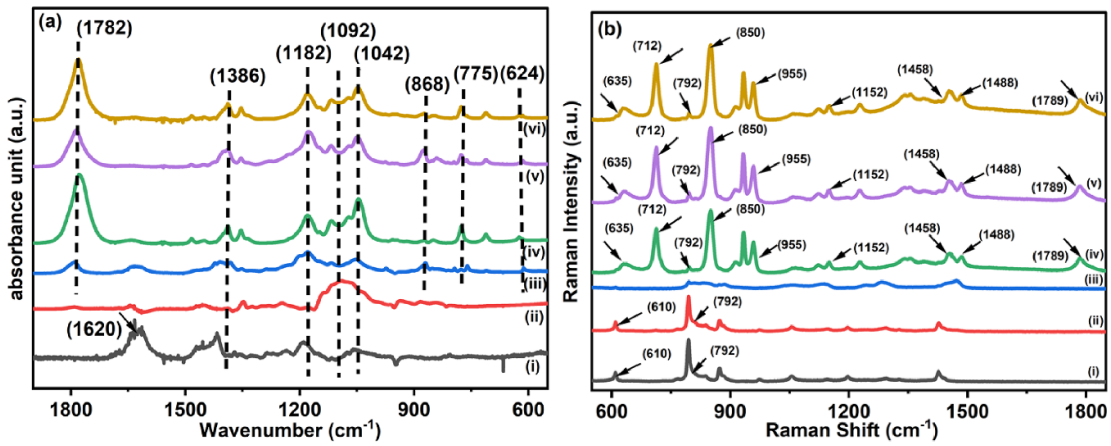

Figure 5. (a) FTIR spectra of (i) pure PVDF-HFP, (ii) PVDF-HFP-PEG(4 ml), (iii) PVDF-HFP(4 ml) after PEG removal, (iv) PVDF-HFP-$LiClO_4$, (v) PVDF-HFP-$Mg(ClO_4)_2$, and (vi) PVDF-HFP-$NaClO_4$. (b) Raman spectra of (i) pure PVDF-HFP, (ii) PVDF-HFP-PEG(4 ml),(iii) PVDF-HFP(4 ml) after PEG removal, (iv) PVDF-HFP-$LiClO_4$, (v) PVDF-HFP-$Mg(ClO_4)_2$, and (vi) PVDF-HFP-$NaClO_4$.

information about FTIR and Raman peak assignments, respectively. The FTIR bands associated with PVDF-HFP were distinctly noted at wavenumbers 1182, 1042, 868, and 775 cm^{-1}, which correspond to CF_2 stretching, C–F stretching vibrations/C–F–C symmetric stretching vibrations, CF_2 stretching/C–C symmetric stretching, and C–F stretching, respectively [35, 36]. An intense band at 1092 cm^{-1} appears for the PVDF-HFP-PEG blend and is related to the PEG phase. This peak almost vanishes in the spectra recorded for PVDF-HFP-$LiClO_4$, PVDF-HFP-$Mg(ClO_4)_2$, and PVDF-HFP-$NaClO_4$ electrolytes, indicating the successful extraction of PEG during soaking of the membrane in methanol. In the case of pure PVDF-HFP, the sharp peak at 1620 cm^{-1} is attributed to the H–O–H bending vibration of absorbed water, indicating the presence of moisture trapped within the porous PVDF-HFP matrix. The bands located at 1782 and 1386 cm^{-1} can be assigned to PC incorporated into the PVDF-HFP matrices with perchlorate salts. Alongside, a signal related to the ClO_4^- ions appears in FTIR spectra at 624 cm^{-1}. This confirms that the ions from the salt are thoroughly integrated within the pores of the PVDF-HFP matrices. The variations in frequency shifting peaks observed in pure PVDF-HFP spectra indicate significant interactions between the polymer, PC as well as perchlorate salts.

FTIR results are further confirmed by the Raman spectra shown in figure 5(b). The Raman spectrum of the pristine PVDF-HFP-PEG exhibits characteristic peaks at 610, 792, and 775 cm^{-1} corresponding to the C–F stretching or CH_2 rocking modes, CH_2 rocking or PEG, respectively [37]. Bands at 1182, 868, and 1042 cm^{-1} correspond to CF_2 stretching, indicating the PVDF-HFP as a host material [38]. The presence of PC in the matrix introduces additional bands around 712, 1152, 1482, 1386, and 1782 cm^{-1} due to C−O bond, CH_2 symmetric stretching, ring breathing, CH_3 symmetrical bending, and C=O bond, respectively [39]. Upon addition of salts $LiClO_4$, $Mg(ClO_4)_2$, $NaClO_4$ into PVDF-HFP matrices, the new peaks emerge at 635 and 955 cm^{-1} [40], indicating interactions between the polymer and perchlorates. Different salts were scaled by the relative intensities changing between ClO_4^- stretching bands (∼1020 cm^{-1}), which represent varying levels of relative dissociation of the ions. The additional peak at 1620 cm^{-1} corresponds to the residual acetone due to −C=O stretching [41]. Similar trends have been found for previously discussed ionic mobility and conductivity measurements. Raman spectroscopy results also reveal that the interactions between the PVDF-HFP matrices and $LiClO_4$, $Mg(ClO_4)_2$, $NaClO_4$ salts are correlated with characteristic peak shifts and intensity variations. Nevertheless, the Raman measurements indicate that the electrolyte with $LiClO_4$ displays the highest ionic dissociation.

3.3. DSC measurements

Figure 6 shows the cooling curve from the DSC measurements recorded for the pure PVDF-HFP and optimized PVDF-HFP after the removal of PEG. table 3 contains the estimated values of crystallization temperature (T_C) and crystallinity (X_C) for those materials. The X_C has been calculated taking into account the heat associated with the melting of the PVDF-HFP and using equation (6):

$$X_c = \frac{\Delta H_M}{\Delta H_M^0} \times 100\% \quad (6)$$

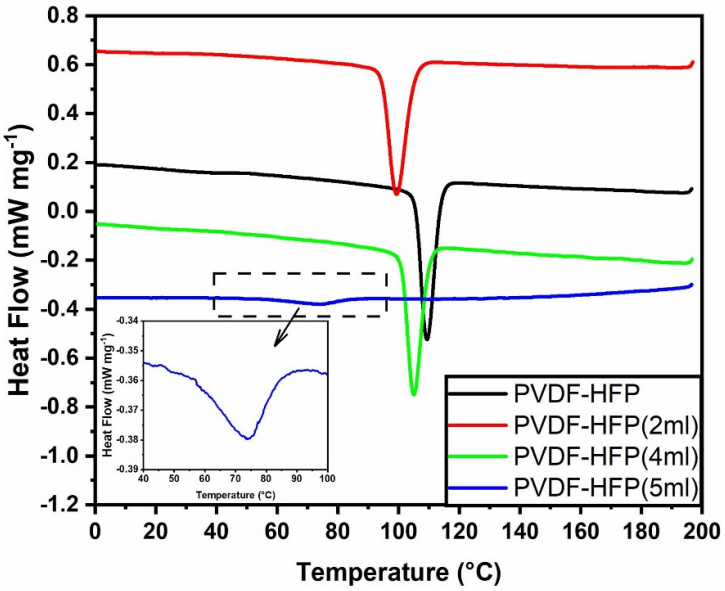

Figure 6. DSC thermograms collected for the pure PVDF-HFP and PVDF-HFP after removal of PEG in cooling mode.

Table 3. Crystallization temperatures (T_C) and the calculated crystallinity (X_C) of bare PVDF-HFP and PVDF-HFP-PEG films.

Sample	T_C (°C)	X_C (%)
PVDF-HFP	109.3	30.1
PVDF-HFP-PEG (2 ml)	99.3	23.7
PVDF-HFP-PEG (4 ml)	105.0	21.8
PVDF-HFP-PEG (5 ml)	73.8	4.4

where ΔH_M is a heat of fusion determined from the area under the DSC melting curve, and $\Delta H_M{}^0$ is a reference heat of fusion of the crystalline α-PVDF phase (104.7 J g^{-1} [42]). Analyzing the obtained results, it is evident that both T_C and X_C decrease for the PVDF-HFP after removal of PEG. This observation is associated with the formation of pores in the PVDF-FHP membranes. It is also worth noting that higher amount of PEG used to prepare membranes lower the crystallinity of them is observed. In other words, the blending of PVDF-HFP with PEG and subsequent removal of PEG causes a progressive amorphization of materials. At the same time, the deterioration of mechanical properties is expected with an increasing content of PEG. DSC measurements showed a reduction in crystallinity after PEG removal, indicating increased amorphous character of the PVDF-HFP matrix. Since ionic transport in polymer electrolytes primarily occurs through amorphous regions via segmental polymer motion, the decrease in crystallinity contributed to enhanced ionic conductivity and improved electrochemical performance. Together, the SEM and DSC findings provide strong structural evidence supporting the enhanced ion transport behavior and superior electrochemical performance observed for the optimized GPEs.

3.4. Mechanical stability of GPEs

The optimized PVDF-HFP GPEs underwent mechanical testing which constitutes a critical evaluation criterion for their practical implementation in device configurations. Mechanical integrity is essential not only for ensuring structural stability during operation but also for maintaining consistent electrochemical performance over time. Figure 7 illustrates the mechanical testing setup and presents the resulting stress–strain curves for three investigated materials: PVDF-HFP-$LiClO_4$, PVDF-HFP-$Mg(ClO_4)_2$, and PVDF-HFP-$NaClO_4$. The samples were made in the form of strips, along with a size of 40 mm in length and ranging from 0.9 to 1 mm in thickness, with a width of 5 mm.

Among the tested samples, PVDF-HFP-$NaClO_4$ demonstrated the greatest mechanical characteristics, with the highest tensile strength and the greatest elongation at break, indicating excellent flexibility. These features suggest a well-connected, dense microstructure that supports uniform stress distribution and efficient load transfer under tensile conditions. In contrast, the PVDF-HFP-$LiClO_4$ GPE showed a modest reduction in both tensile strength and elongation compared with the PVDF-HFP-$NaClO_4$.

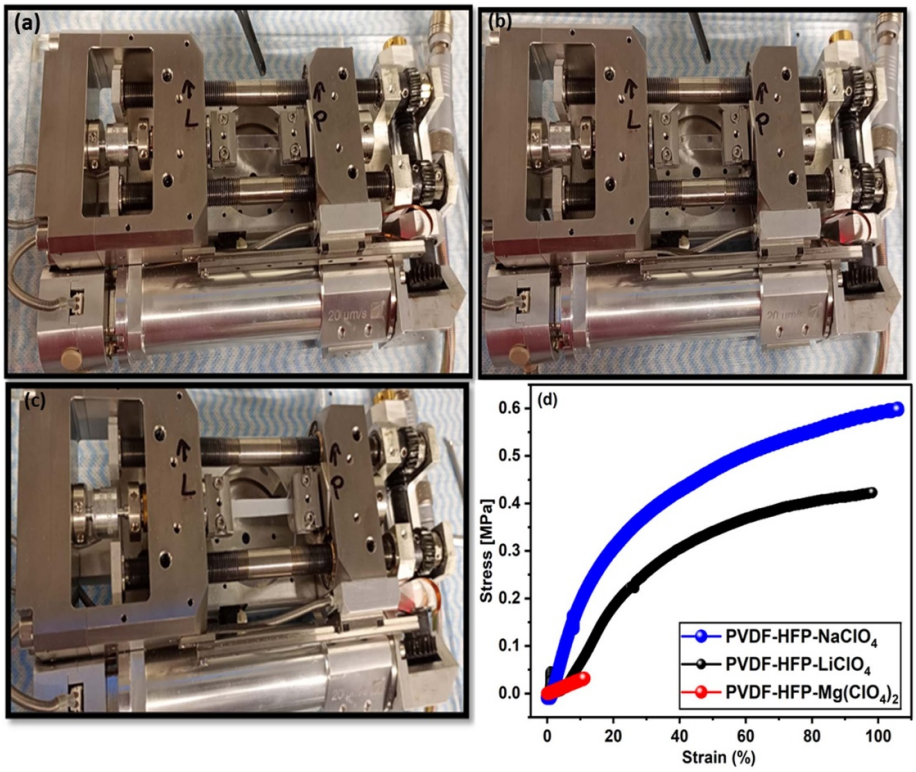

Figure 7. Tensile stress–strain experiments performed for (a) PVDF-HFP-$LiClO_4$, (b) PVDF-HFP-$Mg(ClO_4)_2$, and (c) PVDF-HFP-$NaClO_4$. (d) Stress–strain curves recorded for experiments (a), (b), and (c).

Nevertheless, the mechanical properties remain within an acceptable range for practical applications, implying that the polymer-salt interaction and phase morphology are still sufficient to support mechanical functionality.

On the other hand, PVDF-HFP-$Mg(ClO_4)_2$ exhibited a significant reduction in both tensile strength and strain, indicating poor mechanical behavior. This pronounced degradation in mechanical performance can be directly attributed to the porous morphology observed in its microstructure. The presence of pores compromises the structural continuity of the material, creating localized stress concentrations that lead to premature failure under tensile loading. These observations are in good agreement with SEM and DSC results.

3.5. Electrochemical testing in SC mode

To check if the ESW established during the LSV measurements is valid for Cells A–C, the CV studies have also been performed for them at different scan rates from 5 to 100 mV s^{-1} and in the potential range up to 2.6 V. The obtained results are shown in figures 8(a)–(c). In general, all the cells show a stable performance in this voltage range. They show a box-like curve, which confirms the EDLC energy storage mechanism. The capacitance values have been calculated using equation S5 (provided in the supplementary materials). The single electrode specific capacitance of Cells A-C reaches 132.8, 59.6, and 59.9 F g^{-1}, respectively, showing that the best performance is found for the Li-based cell. It is related to the fact that Li^+ ions possess a lower ionic radius than Mg^{2+} and Na^+ ions, which facilitates the ion mobility and decreases resistance at higher currents. Figure 8(d) presents the variation of specific capacitance with respect to different scan rates for Cells A-C. The increase in scan rates causes a decrease in capacitance values due to the rapid movement of electrolyte ions into the framework of electrode materials.

The EIS measurements were recorded for the Cells A–C to determine the bulk resistance (R_b), charge transfer resistance (R_{ct}) that is taking place at the electrode–electrolyte interface. The EIS spectra are shown in figure 9(a). At the high frequency region, all cells display semi-circular arcs representing the charge transfer process at the electrode–electrolyte interface. The estimated values of R_b and R_{ct} for Cells A–C, along with the calculated capacitance values, are summarized in table 4. From the Nyquist representation of EIS results, it can be clearly seen that Cell A shows the lowest total resistance, with a bulk

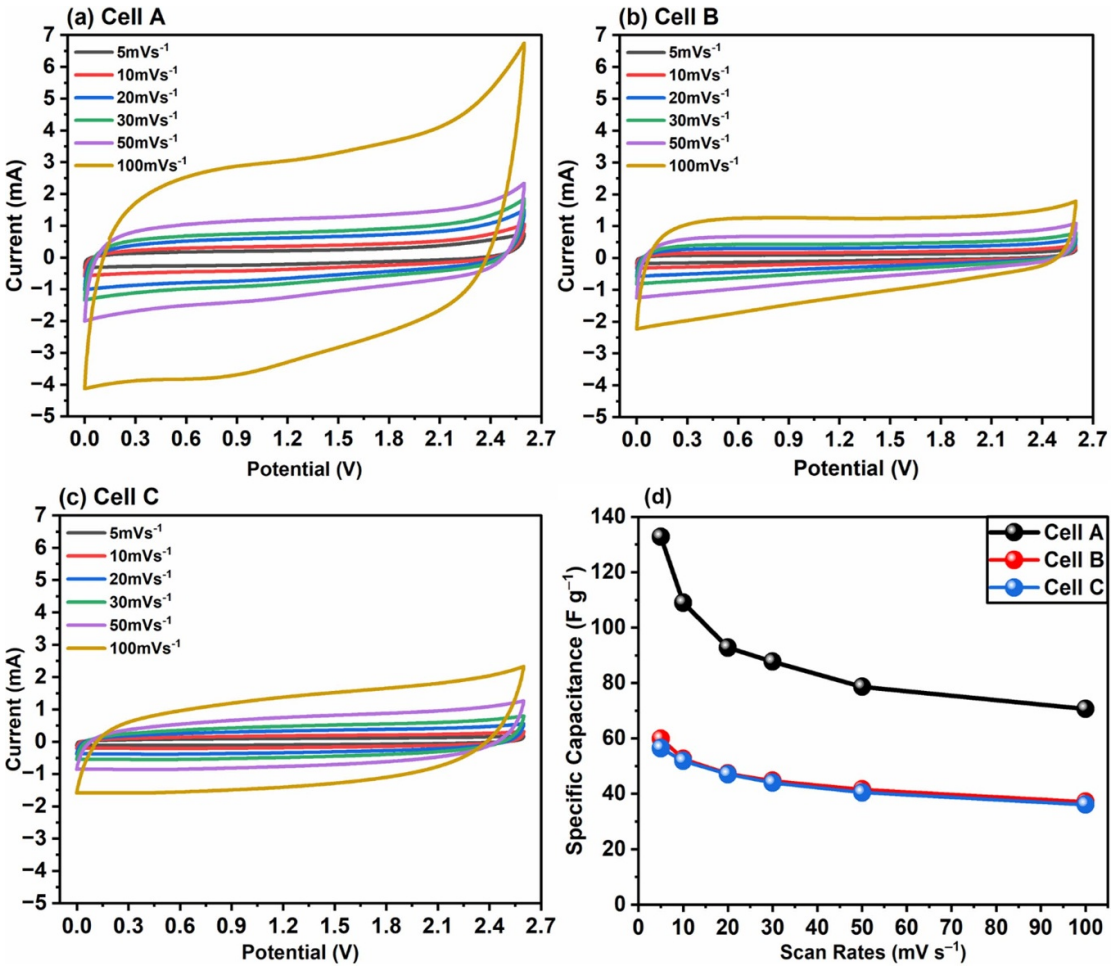

Figure 8. CV curves recorded for (a) cell A, (b) cell B, and (c) cell C at different scan rates ranging from 5 to 100 mV s^{-1} and voltage window from 0 to 2.6 V; (d) variation of specific capacitance of cells A-C with respect to various scan rates at a voltage window ranging from 0 to 2.6 V.

resistance (R_b) of 3.9 Ω and charge transfer resistance (R_{ct}) of 14.6 Ω, confirming the ionic conductivity of the Li^+ based system due to a small ionic radius of Li^+. Cell A also exhibits the steepest slope at the low frequency region, indicating rapid ion diffusion kinetics. Cells B and C reveal larger semicircles, with R_b/R_{ct} values of 4.3/17.3 Ω and 8.5/18.8 Ω, respectively, reflecting the increased ionic friction and interfacial polarization effects associated with Mg^{2+} and Na^+ transport. Cell A maintains the most ideal capacitive behavior. The single electrode specific capacitance values of the Cells A–C were calculated by using equation S1 as provided in the supplementary materials.

Figure 9(b) shows the GCD curves of Cells A–C. The studies have been recorded at a current density of 1 A g^{-1} and the voltage range from 0 to 2.6 V. As can be seen, the GCD curves exhibit the typical triangular shape, which confirms the capacitive-like behavior of all cells. The single electrode specific capacitance values of Cell A, Cell B, and Cell C are 76.7, 54.4, and 49.4 F g^{-1}, respectively (calculated using equation (S2), provided in the supplementary materials), which are in line with the values obtained from the EIS measurements. The energy and power density of Cells A–C have also been calculated using equations S3 and S4 (provided in the supplementary materials), and it is found to be in the order of 124.7, 56.3, and 53.1 Wh kg^{-1} and 2,390, 1,079, and 1,017 W kg^{-1}, respectively. Figure 9(c) shows the variation of specific capacitance of Cells A–C with respect to current density from 0.25 to 5.0 A g^{-1}. As can be seen, the values of specific capacitance decrease with increasing current densities. Table 5 highlights the excellent electrochemical performance of PVDF-HFP-$LiClO_4$ studied in this work against other GPEs used in the EDLCs in terms of specific capacitance, ionic conductivity, energy density, and power density. In turn, figure 9(d) shows the long-term cycling stability tests and cell and estimated coulombic efficiency (CE) for Cells A-C at ESW of 2.6 V. As can be seen, Cell A reveals exceptional durability, maintaining 74.3 F g^{-1} after 10 000 cycles (~96.9% retention from its initial 76.7 F g^{-1}). In contrast, Cells B and C exhibit lower but stable capacitance values, namely, 33.9 F g^{-1} and 33.3 F g^{-1}, respectively, confirming their inferior charge storage efficiency. CE values calculated using

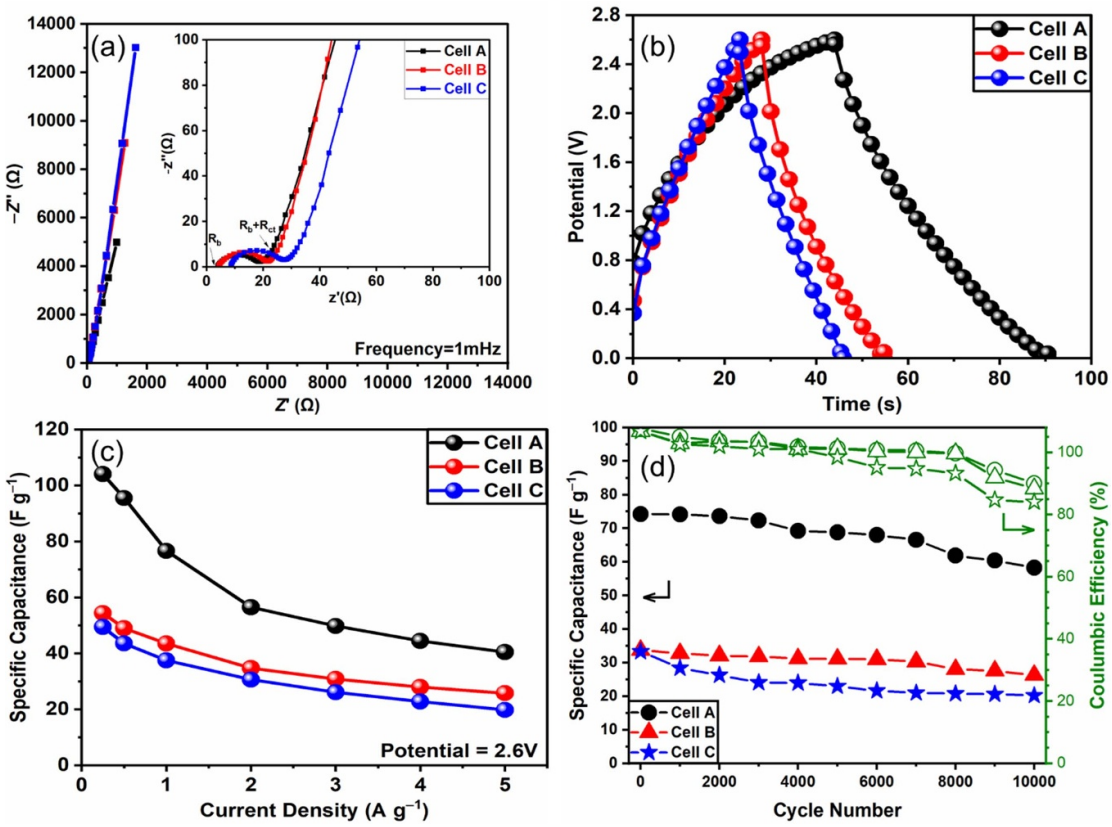

Figure 9. (a) EIS plots of cells A–C; (b) GCD curves of cells A–C recorded at a current density of 1 A g^{-1}; (c)variation of specific capacitance of cells A–C with respect to various current densities ranging from 0.25 to 5 A g^{-1}; (d) long-term cycling and coulombic efficiency of cells A–C collected at 1 A g^{-1} and voltage window from 0 to 2.6 V.

Table 4. Resistance and capacitance values from EIS recorded for Cells A–C.

Cell	R_b [Ω]	R_{ct} [Ω]	C [F g^{-1}]
Cell A	3.9	14.6	99.1
Cell B	4.3	17.3	37.9
Cell C	8.5	18.8	31.1

equation S6 (provided in the supplementary materials) for all the Cells indicate that Cell A maintains efficiency at 100% up to the 7000th cycle, which then gradually decreases to 90.1% at 10 000th cycle. The observed gradual decline in CE after prolonged cycling is likely associated with cumulative interfacial degradation processes occurring at the relatively high operating voltage of 2.6 V. Possible contributing mechanisms include slow electrolyte decomposition, minor parasitic faradaic reactions at the electrode–electrolyte interface, gradual structural changes within the porous polymer matrix, and partial electrolyte depletion over extended cycling. Nevertheless, the capacitance retention remained high (∼96.9%), indicating that the degradation process is relatively limited. In turn, Cell B and Cell C reach around 100% of CE only up to the 5000th cycle, and then drop to 88.5% and 84.1% at the 10 000th cycle, respectively. The great performance of $LiClO_4$-based electrolyte underscores its potential for high-voltage energy storage, driven by the optimal balance of ionic conductivity, charge transfer kinetics, structural stability, and excellent cycling stability.

4. Conclusion

In conclusion, the successful development of GPEs, which are based on the PVDF-HFP matrices filled with lithium, sodium, and magnesium perchlorates dissolved in PC, for their application in EDLCs. Porous PVDF-HFP-based GPEs were successfully developed using a PEG-assisted pore-forming strategy followed by incorporation of perchlorate salts. The results demonstrate that controlled porosity significantly enhances electrolyte uptake and ionic transport. The initial electrochemical characterization of the

Table 5. Comparison of polymer electrolytes in terms of their ionic conductivity, energy density, and power density.

Electrolyte	Ionic conductivity (S cm−1)	Energy density (Wh kg−1)	Power density (W kg−1)	References
PVDF-HFP-PMMA	2.7×10^{-3}	31.42	1250	[36]
PVDF-HFP-EC-PC-Al_2O_3-$TEABF_4$	6.04×10^{-3}	2.97	1064	[43]
PVA-LO-$LiClO_4$	3.06×10^{-3}	97.3	1200	[44]
PVA-KOH	5.55×10^{-3}	7.8	15 340	[45]
Py/GO-RuO_2	1.61×10^{-2}	—	—	[46]
PVDF-HFP-PAN-N-doped carbon quantum dots	—	42.88	19 300	[47]
Poly(VA-co-AN) (PEO-30%IL-20/1$LiBF_4$)	4×10^{-4}	61	500	[48]
PVA-PVP-NaSCN-$LiClO_4$	8.1×10^{-5}	—	—	[49]
PEO-PVP-V_2O_5	2.62×10^{-8}	2.5	494	[50]
PVdF-HFP-SN-EMPTFSI-LiTFSI	—	80.5	70.6	[51]
$NaClO_4$-EC:PC-PVdF-HFP	0.008×10^{-3}	—	—	[52]
PVDF-HFP-Zn$(CF_3SO_3)_2$-Pyr_{13}TFSI	1.52×10^{-3} S cm^{-1}	—	—	[53]
PVDF-HFP-PC-$LiClO_4$	7.4×10^{-3}	124.7	2390	This work

investigated electrolyte materials proves the highest ionic conductivity of the lithium-based GPE and a large ESW of 2.6 V, both being very important for charge transport and stable working over a wide voltage range. The tensile tests confirm the sufficient mechanical properties of polymers filled with Na and Li salts. Cell A containing $LiClO_4$ achieves a specific capacitance of 76.7 F g^{-1} at a single electrode measured at 1 A g^{-1}. Additionally, Cell A maintains high stability for approximately 10000 GCD cycles at a current density of 1 A g^{-1} with 90.1% CE at 10 000th cycle. Cells B and C demonstrate single electrode specific capacitance values of 54.4 and 49.4 F g^{-1} with lower CE, respectively, measured at the same conditions. Among the three cells, Cell A exhibits the most promising electrochemical performance, as demonstrated by EIS, CV, and GCD analyses. The current study shows that by combining controlled pore engineering with targeted salt selection, this work achieves a balanced enhancement in ionic conductivity, electrochemical stability, and cycling durability, offering a promising pathway for high-voltage solid-state SCs.

Acknowledgment

The authors would like to thank Professor Andrzej Wysmołek from the Faculty of Physics University of Warsaw for providing access to the Raman spectrometer. This work was financially supported by the National Centre for Research and Development (NCBR, Poland); Project number: V4-Japan/2/17/AtomDeC/2022.

Data availability statement

The data that support the findings of this study are available upon reasonable request from the authors. The data underlying this study are not publicly available because they contain confidential/proprietary information and are subject to institutional restrictions on public dissemination. Therefore, the data cannot be deposited in a public repository. The data can, however, be made available from the corresponding author upon reasonable request, subject to approval and any applicable restrictions.

Supplementary Information available at https://doi.org/10.1088/2053-1591/ae7e4e/data1.

Conflict of interest

The authors declare that they have no known competing financial interests or personal relationships that could have appeared to influence the work reported in this paper.

Author contributions

Janhavi Sharma
Formal analysis (lead), Investigation (lead), Validation (lead), Visualization (lead)

Marcin Krajewski 0000-0002-4486-2978
Conceptualization (equal), Formal analysis (equal), Investigation (supporting), Methodology (equal), Supervision (equal), Visualization (supporting)

Chandra Shekhar 0000-0002-4665-2915
Validation (supporting), Writing – original draft (supporting), Writing – review & editing (supporting)

Kamil Bochenek
Investigation (supporting), Validation (supporting), Writing – original draft (supporting), Writing – review & editing (supporting)

Angelika Zaszczyńska
Investigation (supporting), Validation (supporting), Writing – review & editing (supporting)

Emerson Coy
Investigation (supporting), Writing – review & editing (supporting)

Marcin Jarek
Investigation (supporting), Writing – review & editing (supporting)

Zhi-Ting Huang 0000-0003-0448-3380
Investigation (supporting)

Amrita Jain 0000-0001-7657-8974
Conceptualization (equal), Formal analysis (equal), Funding acquisition (lead), Methodology (equal), Supervision (equal), Writing – original draft (equal), Writing – review & editing (equal)

References

[1] Elalfy D A, Gouda E, Kotb M F, Bureš V and Sedhom B E 2024 Comprehensive review of energy storage systems technologies, objectives, challenges, and future trends *Energy Strategy Rev.* **54** 101482
[2] Zhu Y, Keoleian G A and Cooper D R 2025 The role of hydrogen in decarbonizing U.S. industry: a review *Renew. Sustain. Energy Rev.* **214** 115392
[3] Sun C, Li Y, Li M, Sun Z, Yuan X, Jin H and Zhao Y 2024 Ferroelectrics enhanced electrochemical energy storage system *Energy Storage Mater.* **70** 103456
[4] Wang G, Zhang L and Zhang J 2012 A review of electrode materials for electrochemical supercapacitors *Chem. Soc. Rev.* **41** 797–828
[5] Jiang H, Lee P S and Li C 2013 3D carbon-based nanostructures for advanced supercapacitors *Energy Environ. Sci.* **6** 41–53
[6] Zhou D, Shanmukaraj D, Tkacheva A, Armand M and Wang G 2019 Polymer electrolytes for lithium-based batteries: advances and prospects *Chem* **5** 2326–52
[7] Mindemark J, Lacey M J, Bowden T and Brandell D 2018 Beyond PEO—alternative host materials for Li+-conducting solid polymer electrolytes *Prog. Polym. Sci.* **81** 114–43
[8] Jie J, Liu Y, Cong L, Zhang B, Lu W, Zhang X, Liu J, Xie H and Sun L 2020 High-performance PVDF-HFP based gel polymer electrolyte with a safe solvent in Li metal polymer battery *J. Energy Chem.* **49** 80–88
[9] Wang J, Li X, Yang J, Sun W, Ban Q, Gai L, Gong Y, Xu Z and Liu L 2021 Flame-retardant, highly conductive, and low-temperature-resistant organic gel electrolyte for high-performance all-solid supercapacitors *ChemSusChem* **14** 2056–66
[10] Stephan A M and Nahm K S 2006 Review on composite polymer electrolytes for lithium batteries *Polymer* **47** 5952–64
[11] Wu Y, Li Y, Wang Y, Liu Q, Chen Q and Chen M 2022 Advances and prospects of PVDF based polymer electrolytes *J. Energy Chem.* **64** 62–84
[12] Mathies L, Diddens D, Dong D, Bedrov D and Leipner H 2020 Transport mechanism of lithium ions in non-coordinating P(VdF-HFP) copolymer matrix *Solid State Ion.* **357** 115497
[13] Laxmayyaguddi Y, Mydur N, Pawar A S, Hebri V, Vandana M, Sanjeev G and Hundekal D 2018 Modified thermal, dielectric, and electrical conductivity of PVDF-HFP/LiClO4 polymer electrolyte films by 8 MeV electron beam irradiation *ACS Omega* **3** 14188–200
[14] Armand M, Endres F, MacFarlane D R, Ohno H and Scrosati B 2009 Ionic-liquid materials for the electrochemical challenges of the future *Nat. Mater.* **8** 621–9
[15] Tsai C Y, Peng K J, Wang C F and Liu Y L 2019 Creation of lithiumion-conducting channels in gel polymer electrolytes through non-solvent-induced phase separation for high-rate lithium-ion batteries *ACS Sustain. Chem. Eng.* **8** 2138–46
[16] Zhang J, Larrañaga A L, Yang F, Jiang W, Hu M, Sui S, Li H and Jiang F 2024 Tailoring porous structure in non-ionic polymer membranes using multiple templates for low-cost iron-lead single-flow batteries *Energy Mater.* **4**
[17] Kim J-H and Lee K-H 1998 Effect of PEG additive on membrane formation by phase inversion *J. Membr. Sci.* **138** 153–63
[18] Shi L, Wang R, Cao Y, Feng C, Liang D T and Tay J H 2007 Fabrication of poly(vinylidene fluoride-co-hexafluropropylene) (PVDF-HFP) asymmetric microporous hollow fiber membranes *J. Membr. Sci.* **305** 215–25
[19] Park H-H, Lim C-W, Jo H-D, Choi W-K and Lee H-K 2007 Absorption of SO2 using PVDF hollow fiber membranes with PEG as an additive *Korean J. Chem. Eng.* **24** 693–7
[20] Evans J, Vincent C A and Bruce P G 1987 Electrochemical measurement of transference numbers in polymer electrolytes *Polymer* **28** 2324–8
[21] Hasegawa G, Kanamori K, Kiyomura T, Kurata H, Abe T and Nakanishi K 2016 Hierarchically porous carbon monoliths comprising ordered mesoporous nanorod assemblies for high-voltage aqueous supercapacitors *Chem. Mater.* **28** 3944–50

[22] Lee W S V, Xiong T, Loh G C, Tan T L and Xue J 2018 Optimizing electrolyte physiochemical properties toward 2.8 V aqueous supercapacitor *ACS Appl. Energy Mater.* **1** 3070–76
[23] Winter M and Brodd R J 2004 What are batteries, fuel cells, and supercapacitors? *Chem. Rev.* **104** 4245–70
[24] Zhu J, Zhang Z, Zhao S, Westover A S, Belharouak I and Cao P F 2021 Single-ion conducting polymer electrolytes for solid-state lithium–metal batteries: design, performance, and challenges *Adv. Energy Mater.* **11** 2003836
[25] Jeschull F, Hub C, Kolesnikov T I, Sundermann D, Hernández G, Voll D, Mindemark J and Théato P 2024 Multivalent cation transport in polymer electrolytes—reflections on an old problem *Adv. Energy Mater.* **14** 230274510
[26] Zhong C, Deng Y, Hu W, Qiao J, Zhang L and Zhang J 2015 A review of electrolyte materials and compositions for electrochemical supercapacitors *Chem. Soc. Rev.* **44** 7484–539
[27] Sun Y, He Y, Sheha E, Yang J, Wang J and NuLi Y 2025 Developing single-ion conductor polymer electrolytes for rechargeable magnesium batteries: a concept *ChemSusChem* **18** e202402732 [In German]
[28] Pavithra S, Sakunthala A, Rajesh S, Kavitha S and Sathishkumar P 2023 Influence of graphene oxide on the membrane characteristics of PVDF-HFP as an electrolyte for lithium-based energy storage devices *Appl. Nanosci.* **13** 4177–92
[29] Jayanthi S 2019 Studies on ionic liquid incorporated polymer blend electrolytes for energy storage applications *Adv. Compos. Hybrid Mater.* **2** 351–60
[30] Shan X, Song Z, Ding H, Li L, Tian Y, Sokolov A P, Tian M, Xu K and Cao P-F 2024 Polymer electrolytes with high cation transport number for rechargeable Li-metal batteries: current status and future direction *Energy Environ. Sci.* **17** 8457–81
[31] Marchiori C F N, Carvalho R P, Ebadi M, Brandell D and Araujo C M 2020 Understanding the electrochemical stability window of polymer electrolytes in solid-state batteries from atomic-scale modeling: the role of Li-ion salts *Chem. Mater.* **32** 7237–46
[32] Yang Q, Huang J, Li Y, Wang Y, Qiu J, Zhang J, Yu H, Yu X, Li H and Chen L 2018 Surface-protected $LiCoO_2$ with ultrathin solid oxide electrolyte film for high-voltage lithium ion batteries and lithium polymer batteries *J. Power Sources* **388** 65–70
[33] Gupta A *et al* 2021 Hydrogen clathrates: next generation hydrogen storage materials *Energy Storage Mater.* **41** 69–107
[34] Li Y, Zhao X, Bao Q, Cui M, Qiu W and Liu J 2020 How inactive d0 transition metal controls anionic redox in disordered Li-rich oxyfluoride cathodes *Energy Storage Mater.* **32** 253–60
[35] Guo Z and Lin Q 2014 Coupling reaction of CO2 and propylene oxide catalyzed by DMC with co-complexing agents incorporated via ball milling *J. Mol. Catal. A* **390** 63–68
[36] Yang W, Li L, Zhang B, Yang Q, Zou H, Zheng W and Chen S 2021 Optimization and preparation of a gel polymer electrolyte membrane for supercapacitors *Chem. Eng. Technol.* **44** 449–56
[37] Constantino C J L, Job A E, Simões R D, Giacometti J A, Zucolotto V, Oliveira O N Jr and G Gozz D L 2005 Chinaglia "phase transition in poly(vinylidene fluoride) investigated with micro-Raman spectroscopy *Appl. Spectrosc.* **59** 275–9
[38] Janakiraman S, Agrawal A, Biswal R and Venimadhav A 2021 An amorphous polyvinylidene fluoride-co-hexafluoropropylene based gel polymer electrolyte for sodium-ion cells *Appl. Surf. Sci. Adv.* **6** 100139
[39] Ostrovskii D, Torell L M, Appetecchi G B and Scrosati B 1998 An electrochemical and Raman spectroscopical study of gel polymer electrolytes for lithium batteries *Solid State Ion.* **106** 19–24
[40] Qu H, Ling Z, Qi X, Xin Y, Liu C and Cao H 2021 A remote Raman system and its applications for planetary material studies *Sensors* **21** 6973
[41] Javed H, Islam A, Chauhan A, Kumar S and Kumar S 2021 Efficacy of engineered GO Amberlite XAD-16 picolylamine sorbent for the trace determination of Pb (II) and Cu (II) in fishes by solid phase extraction column coupled with inductively coupled plasma optical emission spectrometry *Chem. Eng. Technol.* **44** 449–56
[42] Krajewski M, Witowski A M, Liou S C, Maj M, Tokarczyk M and Wasik D 2023 Poly(vinylidene fluoride-co-hexafluoropropylene) films filled in iron nanoparticles for infrared shielding applications *Macromol. Rapid Commun.* **44** 2300038
[43] Tripathi M, Bobade S M and Kumar A 2021 Nanocomposite polymer gel with dispersed alumina as an efficient electrolyte for application in supercapacitors *J. Phys. Chem. Solid* **152** 109944
[44] Lin Y H, Huang W-T, Huang Y-T, Jhang Y-N, Shih T-T, Yilmaz M and Deng M-J 2023 Evaluation of polymer gel electrolytes for use in MnO2 symmetric flexible electrochemical supercapacitors *Polymers* **15** 3438
[45] Yu H, Wu J, Fan L, Xu K, Zhong X, Li Y and Lin J 2011 Improvement of the performance for quasi-solid-state supercapacitor by using PVA-KOH-KI polymer gel electrolyte *Electrochim. Acta* **56** 6881–6 [In French]
[46] Ping Z, XiaoJing L, Anye R and Peng G 2016 Preparation of a novel porous gel electrolyte and its application in micro supercapacitor *J. Electroanal. Chem.* **782** 154–60
[47] Bai Y, Yang C, Yuan B, Li H, Chen W, Yin H, Zhao B, Shen F and Han X 2023 A UV cross-linked gel polymer electrolyte enabling high-rate and high voltage window for quasi-solid-state supercapacitors *J. Energy Chem.* **76** 41–50
[48] Karaman B, Çevik E and Bozkurt A 2019 Novel flexible Li-doped PEO/copolymer electrolytes for supercapacitor application *Ionics* **25** 1773–81
[49] Badi N, Theodore A M, Alghamdi S A, Al-aoh H A, Lakhouit A, Roy A S, Alatawi A S and Ignatiev A 2022 Fabrication and characterization of flexible solid polymers electrolytes for supercapacitor application *Polymers* **14** 3837
[50] Maria Therease Ramya W, Siva V, Murugan A, Shameem A, Jothi M A, Hussein M, Venkatachalam K and Kumar K A 2025 Nanoscale V2O5 anchored biodegradable PVP/PEO based polymer nanocomposites for flexible supercapacitor applications *J. Mol. Liq.* **422** 126908
[51] Bhat M Y and Hashmi S A 2022 Mixture of non-ionic and organic ionic plastic crystals immobilized in poly (vinylidene fluoride-co-hexafluoropropylene): a flexible gel polymer electrolyte composition for high performance carbon supercapacitors *J. Energy Storage* **51** 104514
[52] Yadav A, Hashmi S A, Kumari P and Mohd Sadiq A G 2026 Sustainable apricot leaves derived activated carbon as an efficient electrode material with different electrolytes for high-performance electric double-layer capacitors *J. Energy Storage* **161** 121922
[53] Liu J, Ahmed S, Wang T and Song S 2023 Flexible thermotolerant Zn-ion hybrid supercapacitors enabled by heat-resistant polymer electrolyte *Chem. Eng. J.* **451** 138512